university of groningen / faculty of science and engineering

Molecule Number Determination of BaF in the NL-eEDM Experiment

Author:
Konstantinos GKINOPOULOS
(s4082346)

Supervisor:
prof./ dr. Lorenz WILLMANN
Second examiner :
prof./ dr. Steven JONES

Bachelor's Thesis
To fulfill the requirements for the degree of
Bachelor of Science in Physics
at the University of Groningen

July 18, 2025

Contents

Abstract

This thesis discusses a new detection scheme proposed for the molecular number determination of barium monofluorine (BaF) in the NL-eEDM experiment. It presents the first experimental observation of the $X^2\Sigma(N=0) \rightarrow D^2\Sigma^+(N=1)$ transition in BaF, a significant milestone in the spectroscopic investigation of this molecule. The transition was detected using laser-induced fluorescence in the molecular beam of the NL-eEDM setup, allowing for the confirmation of the theoretical predictions concerning hyperfine structure and state-selective excitation. This transition was observed at a frequency of 739.94638 THz with a hyperfine splitting of 66.4 ± 1.1 MHz for the $X^2\Sigma^+$ ground state , consistent with the theoretical expectation of 65.9 MHz . A Voigt profile analysis was used to extract the convolution between the Lorentzian and the Gaussian contributions to the observed spectrum. Despite limitations in the laser intensity and optical beam quality, the measurements revealed the hyperfine splitting ($F = 1 \rightarrow F = 2$) of the excited $D^2\Sigma^+_{3/2}$ state at 5.3 ± 1.3 MHz. A theoretical saturation intensity was calculated, while Doppler broadening was observed under near perpendicular laser beam geometry. Challenges such as limited signal-to-noise ratio, reduced photon efficiency and large shot to shot molecular number variations are discussed. This thesis outlines key improvements necessary for future precision measurements within the framework of the NL-eEDM experiment.

Acknowledgments

I would like to express my deepest gratitude to my supervisor, Lorenz, for his guidance, shared knowledge, support, and all the advice he generously offered whenever I needed it. His clear explanations and deep understanding have undoubtedly contributed to both my learning and the development of this thesis — as well as to the many enjoyable conversations we had along the way.
I also wish to thank Steven, my other supervisor, for his theoretical input and for providing constructive feedback on my work.
A special thanks goes to the entire NL-eEDM collaboration team — especially Jelmer and Oliver — for their help with the laser setup, for always being open to questions, and for contributing to such a welcoming and enjoyable working environment.
Last but not least, I would like to personally thank Bastiaan for the many insightful discussions we had, his technical assistance, and the clear, patient explanations he provided throughout this project. His help was truly invaluable at every stage. His constant availability and willingness to help — often on short notice — made a huge difference. I truly appreciated his support, and I wish him all the best in completing his PhD thesis and in all his future endeavors.

1 Introduction

In 1950, E. M. Purcell and N. F. Ramsey posed a deceptively simple but deeply consequential idea: the neutron might possess an electric dipole moment (EDM) [1]. At the time, this proposal challenged the prevailing understanding of fundamental symmetries in particle physics and was quickly dismissed. Interest in this idea grew significantly again in 1956 when it was discovered that weak interactions violate parity symmetry (P) [2]. In 1957, motivated by these developments, Purcell and Ramsey, together with their student, J. H. Smith, officially published the first dedicated experimental search for a neutron EDM, initiating what would become a major effort to detect non-zero EDMs [3].

The sequence of particle discoveries that followed, leading to the 1960s, laid the groundwork for the development of the Standard Model (SM) of Particle Physics. According to the SM, any local, energy-positive, Lorentz-invariant quantum field theory must conserve a fundamental symmetry known as CPT symmetry [4]. The initials correspond to Charge conjugation (C), Parity transformation (P), and Time reversal (T). Since the combined operations of CPT are expected to leave a system invariant, breakdown of CP invariance should be accompanied by a violation of time - reversal (T) symmetry. Therefore, there is a reason to expect that EDMs should exist at some level [5]. In particular, the SM already predicts a small amount of CP violation, leading to a very small upper limit for the value of eEDM: $d_e \sim 10^{-35}\ e \cdot \text{cm}$ [6]. While this CP violation has been experimentally observed in the decay of certain mesons, such as kaons [7] and B-meson decays [8], the extend of the violation predicted falls several orders of magnitude short. Additional CP violation is required to explain the observed asymmetry between matter and antimatter in the Universe. Theoretical models like supersymmetry (SUSY) attempt to explain physics beyond the SM by introducing additional sources of CP violation. These lead to theoretical predictions for the eEDM: $d_e \sim 10^{-27}$ to $\sim 10^{-30}\ e \cdot \text{cm}$, which are accessible to modern precision measurement techniques. Therefore, searching for the eEDM can restrict these new theories and help probe new physics beyond the SM [4].

The first EDM measurement performed on the neutron by Ramsey and Purcell set an upper limit of $d_e < 5 \times 10^{-20}\ e \cdot \text{cm}$. Almost 70 years after that measurement, the upper bound on the EDM has been improved by approximately 10 orders of magnitude. In 2023, the most precise measurement yet of the EDM upper limit using electrons confined inside molecular ions was achieved by the University of Colorado Boulder : $d_e < 4.5 \times 10^{-30}\ e \cdot \text{cm}$ with 90% confidence. This result imposes constraints on new physics arising from time reversal (T)-violating effects at energy scales above 10 TeV [9]. In order to perform the eEDM measurement, the Hamiltonian H of the electron is given as [10]:

$$H = H^0 - (\mu_e \cdot \vec{B} + d_e \cdot \vec{E}_{eff}) \cdot \frac{\vec{S}}{|S|}, \tag{1}$$

where μ_e and d_e are the magnetic and electric dipole moments, respectively. $\vec{B}$ is the applied magnetic field, and $\vec{E_{eff}}$ is the effective internal electric field experienced by the electron, which is significantly enhanced in heavy polar molecules such BaF [11]. A permanent electric dipole moment violates both parity (P) and time-reversal (T) symmetry, because the EDM interaction term $\vec{d_e} \cdot \vec{E_{eff}}$ changes sign under each transformation. Since the electric and magnetic dipole moments are vector quantities, they define a preferred axis in space, which couples to the direction of the spin $\vec{S}$.

1.1 Introduction to the NL-eEDM experiment

The NL-eEDM experiment is located at the University of Groningen, and it is a collaborative effort of a team from the Van Swinderen Institute (VSI) in Groningen with the Vrije Universiteit in Amsterdam, embedded in the Dutch National Institute for particle physics Nikhef. It aims to improve the measurement of the permanent electric dipole moment of the electron (eEDM) using cold molecules. Barium monofluorine (BaF) molecules are chosen due to their favorable molecular properties. The specific reasons for selecting BaF in this experiment are detailed in [11]. The NL-eEDM experiment proposes that a sensitivity of up to $|d_e| < 5 \cdot 10^{-30} e \cdot \mathrm{cm}$ is achieved with the experimental setup discussed in Section 3.

Currently, the setup utilizes the ground state of BaF molecules, which is split into two hyperfine levels: $F = 0$ and $F = 1$. Through optical pumping, population is transferred from the $F = 0$ state to the $F = 1$, where a coherent superposition of the magnetic sublevels $m_F = 1$ and $m_f = -1$ is prepared. This quantum state is given by:

$$|\Psi\rangle = \alpha(|F=1, m_F=+1\rangle - |F=1, m_F=-1\rangle) + \gamma(|F=1, m_F=0\rangle) + \delta(|F=0, m_F=0\rangle),$$

and it evolves over time , accumulating a measurable phase difference ϕ, which is sensitive to the presence of an electric dipole moment.

This phase accumulation arises due to spin precession affected by the electric and magnetic fields. In the presence of a magnetic field, a particle with a magnetic dipole moment experiences a Zeeman shift, however, this coupling to the magnetic field exerts a torque that causes its angular momentum vector to precess, a phenomenon known as Larmor precession. The angular frequency of this precession is proportional to the the magnetic field strength and is given by: $\omega = \gamma \cdot B$, where γ is the gyromagnetic ratio. This precession leads to energy splitting between the $m_f = \pm 1$ sublevels.

Under the assumption that the electron possesses a permanent electric dipole moment, similarly to the coupling observed in the magnetic field, it will couple to the applied electric field in a way that violates parity (P) and time reversal (T) symmetries. As a consequence, an additional shift is introduced in the precession frequency, which depends on the alignment of the electric and magnetic fields. In case where the electric field is reversed, the EDM induced shift also reverses sign, while the magnetic sign contribution remains unchanged. By preparing the same superposition state under opposite electric field directions, a comparison between the resulting phase differences can be achieved. In this comparison, the contribution from the EDM can be isolated. A representation of this description is shown in Figure 1.

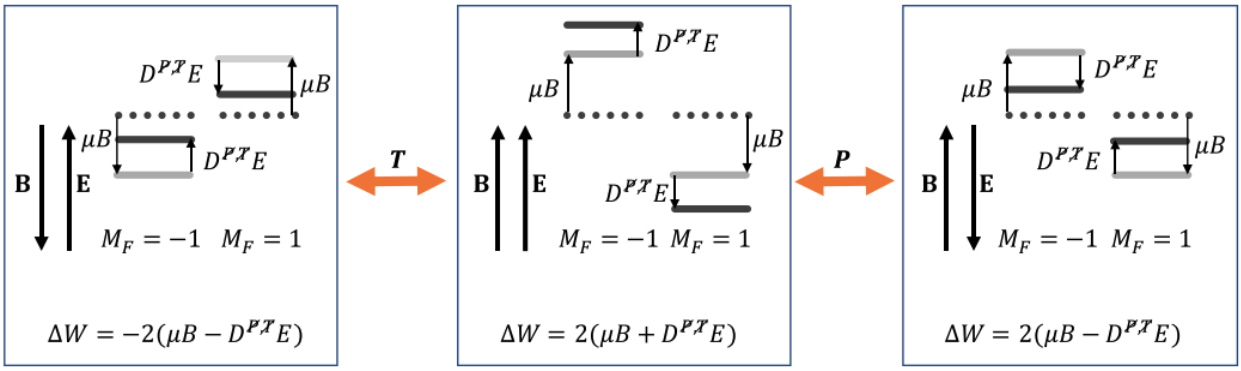

Figure 1: Figure adapted from [12]. The figure shows the energy difference between magnetic sub-levels ($\Delta W = W_{M_F=-1} - W_{M_F=1}$), measured under parallel and anti-parallel configurations of electric and magnetic fields. Reversing the field directions illustrates Time (T) and Parity (P) transformations. Electric field reversal is preferred to avoid magnetic hysteresis. The Zeeman and tensor Stark shifts dominate over the much smaller expected shift from a possible eEDM: $\mu_B \gg D^{P,T}E$ [13]. Not to scale.

1.2 Thesis Motivation

This thesis investigates a new laser detection scheme used to excite BaF molecules from the $X^2\Sigma^+$ ground state to the $D^2\Sigma^+$ excited state. It examines how variations in frequency and laser intensity affect the ability to quantitatively determine the number of molecules detected in the NL-eEDM experiment. By measuring photon counts as a function of laser frequency, the efficiency of excitation can be evaluated, providing insight into how laser parameters impact signal quality and statistical precision.

Until now, BaF molecules have been excited using the $X^2\Sigma^+(N=0) \rightarrow A^2\Pi_{3/2}(J=3/2)$ transition. The laser induced fluorescence (LIF) is collected using photomultiplier tubes (PMTs), which operate via single photon counting to detect individual emitted photons. This particular transition (≈ 815 nm wavelength) is preferred over the $X^2\Sigma^+(N=0) \rightarrow A^2\Pi_{1/2}(J=1/2)$ transition, at 860 nm, as it yields higher photon detection efficiency. A detailed analysis of this detection scheme can be found in [13, Chapter 3].

State sensitivity plays a crucial role in precision measurements of the eEDM. In this experiment, the eEDM is extracted by measuring the spin precession signal, which depends on the population difference between the initial and final hyperfine states. Accurate determination of this population difference requires precision control over the initial state preparation and high efficiency detection over the final state. For that reason, the ability to precisely measure the number of molecules in each state is essential for maximizing signal quality and statistical sensitivity in the NL-eEDM experiment.

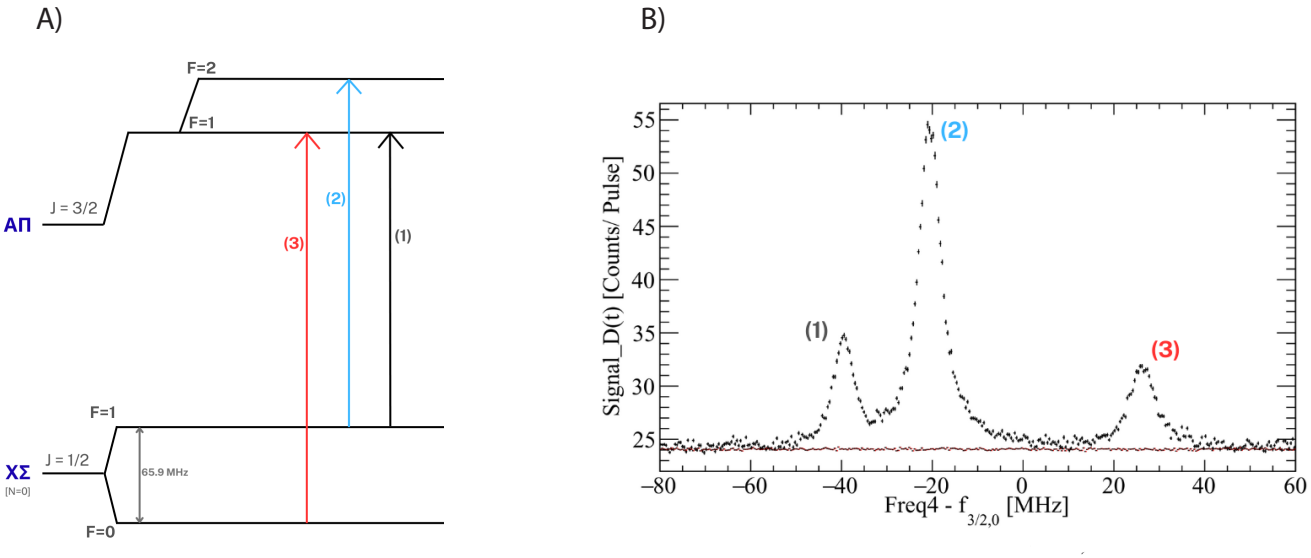

Figure 2: Spectroscopy of the $X^2\Sigma^+(N=0) \rightarrow A^2\Pi_{3/2}(J=3/2)$ transition without optical pumping or spin precession. The observed signal arises from laser-induced fluorescence (LiF) collected using the photomultipliers (PMTs). The frequency is measured with the centroid of the transition subtracted ($f_{3/2} = 367.63214\ THz$). Panel **A** shows the relevant hyperfine structure levels and transitions, while panel **B** presents an example of such measurement. The red points indicate background counts (noise), while the label peaks correspond to transitions from different hyperfine states. Data taken from [13], on the 15th of December 2022.

Figure 2 provides a clear example of this spectroscopy $X^2\Sigma^+(N=0) \rightarrow A^2\Pi_{3/2}(J=3/2)$ transition, recorded without optical pumping or spin precession. The observed signal corresponds to the laser induced fluorescence (LIF). A detailed understanding of this structure is essential for interpreting this LIF signal: The hyperfine levels $F=0$ and $F=1$ in the $X^2\Sigma^+$ ground state are separated by $65.9\ MHz$. Molecules are excited from the ground state to the $F=1$ and $F=2$ hyperfine levels of the $A^2\Pi_{3/2}$ excited state. The transitions in Figure 2A correspond to the peaks shown in Figure 2B. The lifetime of the $A^2\Pi_{3/2}$ state for BaF molecules is $47.9\ ns$ [14]. Such a short lifetime, indicates that fluorescence occurs almost immediately after excitation. According to selection rules, only a small fraction of the excited molecules return to the initial rotational ground state $(N=0)$ [15], making accurate determination of the molecular population more challenging.

While the NL-eEDM experiment primarily focuses on a well defined two-level transition, the actual molecule structure of BaF is much more complex. A visual representation of this structure can be seen in Section 2.1.2. The most important limitation of this detection scheme is that the fluorescence detection has the same wavelength as the excitation and since the PMT, operates in a single-photon counting mode, it detects all incoming photons regardless of their origin. Photons from other decay channels, usually from the excited state to rotational or vibrational levels other than the ground state, contribute also to the detected signal (in terms of background noise). These unwanted decays, occur mainly due to the selection rules and branching ratios of the excited state[16]. Moreover, in the case of LIF detection, PMTs can only detect a few photons per second, due to their high gain and fast response [17, Chapter 6]. As a result, it limits the amount of signal collected. Furthermore, PMTs have an operation restriction know as 'dead time'. 'Dead time' is defines as the period after each photon detection, during which the PMT is unable to register another photon. This dead time is typically

around 10 *ns* [18].

Considering these limitations of the current detection scheme, a new approach has been introduced in the NL-eEDM experiment. Instead of exciting BaF molecules to the $A^2\Pi_{3/2}$ state directly, as was done previously [13, 19], a blue laser at 405 *nm* is used to excite molecules from the ground state $X^2\Sigma^+$ to the $D^2\Sigma^+$ state. The excited molecules then decay from the $D^2\Sigma$ to the $A^2\Pi_{3/2}$ state before returning back to the ground state. This process addresses the problem of the fluorescence detection having the same wavelength as the excitation. The excitation from this new detection scheme occurs via a blue laser at 405 *nm* (in the visible range), while the laser induced fluorescence (LIF) occurs in the same region as before at (≈ 815 *nm*), which means that by blocking the excitation light, background free detection can be achieved.

1.3 Hypothesis

Given the context and motivation outlined in Section 1.2, the following hypothesis is proposed:

The newly introduced detection scheme, based on the excitation of the BaF molecules from the ground state $X^2\Sigma^+$ to the excited state $D^2\Sigma^+$ state, followed by spontaneous decay to the $A^2\Pi_{3/2}$ state and subsequently to the ground state aims to enable background free detection. Assuming that the new laser configuration achieves comparable operational conditions, the total fluorescence signal is expected to remain similar. That is approximately 55 counts as observed in Figure 2B for the $X^2\Sigma$ $(F = 1)$ to $A^2\Pi_{3/2}$ $(F = 2)$ transition. However, by eliminating background signal, which is 25 counts per pulse in Figure 2B, the signal-to-noise ratio (SNR) can be increased (Equation (2)).

According to Equation (3), statistical uncertainty scales inversely with the square root of the number of detected photons [12]. By effectively doubling the SNR, this corresponds to an improvement in statistical uncertainty by a factor of $1/\sqrt{2}$. This enhancement would reduce the data acquisition time required to achieve a given level of statistical uncertainty by half [12].

2 Relevant Theory

This section introduces only the essential physics necessary to understand the content of this thesis. For a more detailed theoretical analysis, references are provided throughout this section.

2.1 Barium Monofluorine (BaF) molecule

2.1.1 Terminology

Component	**Atomic Physics**	**Molecular Physics (Diatomics)**
Term Symbol Format	${}^{2S+1}L_J$	$X^{2S+1}\Lambda_\Omega$
S	Electron spin	Electron spin
L	Orbital angular momentum: spectroscopic notation: S (0), P (1), D (2), etc.	Not a good quantum number; symmetry broken by internuclear axis
J	Total electronic angular momentum: $J = L + S$	Replaced by Ω; total angular momentum is $F = J + I$
Λ	Not used	Projection of orbital angular momentum (m_l) on internuclear axis; $\Sigma, \Pi, \Delta, \ldots$
Ω	Not used	Projection of total electronic angular momentum on internuclear axis: $\Omega = \lvert\Lambda + \Sigma\rvert$
v	Not applicable	Vibrational states: Quantized motion of nuclei along bond axis; vibrational quantum number $v = 0, 1, 2, \ldots$
N	Not applicable	Rotational States : Rotational angular momentum of nuclei; $N = 0, 1, 2, \ldots$
F, m_F	Hyperfine Structure :$F = J + I$; total angular momentum including nuclear spin	Same; includes coupling of nuclear spin I with J, used for state labeling and detection
Additional Labels	-	X: ground state, A, B, C... for excited states

Table 1: Comparison of term symbols and quantum numbers in atomic and molecular physics, including vibrational, rotational, and hyperfine structure relevant to diatomic molecules. Relevant information can be found in: [20, Chapters 5–6]

2.1.2 Molecular Structure

The NL-eEDM experiment uses the molecular energy level structure of the BaF molecule which consists of barium (Ba) with electron configuration $[\mathrm{Xe}]\,6s^2$, and fluorine (F) with configuration $1s^2\,2s^2\,2p^5$. One of the two valence electrons in the barium's $6s$ orbital of the barium is transferred to fluorine, forming an ionic bond. As a result, barium becomes positive charged (Ba^+), and fluorine becomes negatively charged (F^-).

Since all atomic orbital (core and valence) are filled in both ions after bonding, the only remaining unpaired electron resides in barium's $6s$ orbital. It is these lone unpaired electrons whose spin precession will be measured in this experiment. The structure of the BaF for the ground level can be seen in Figure 3.

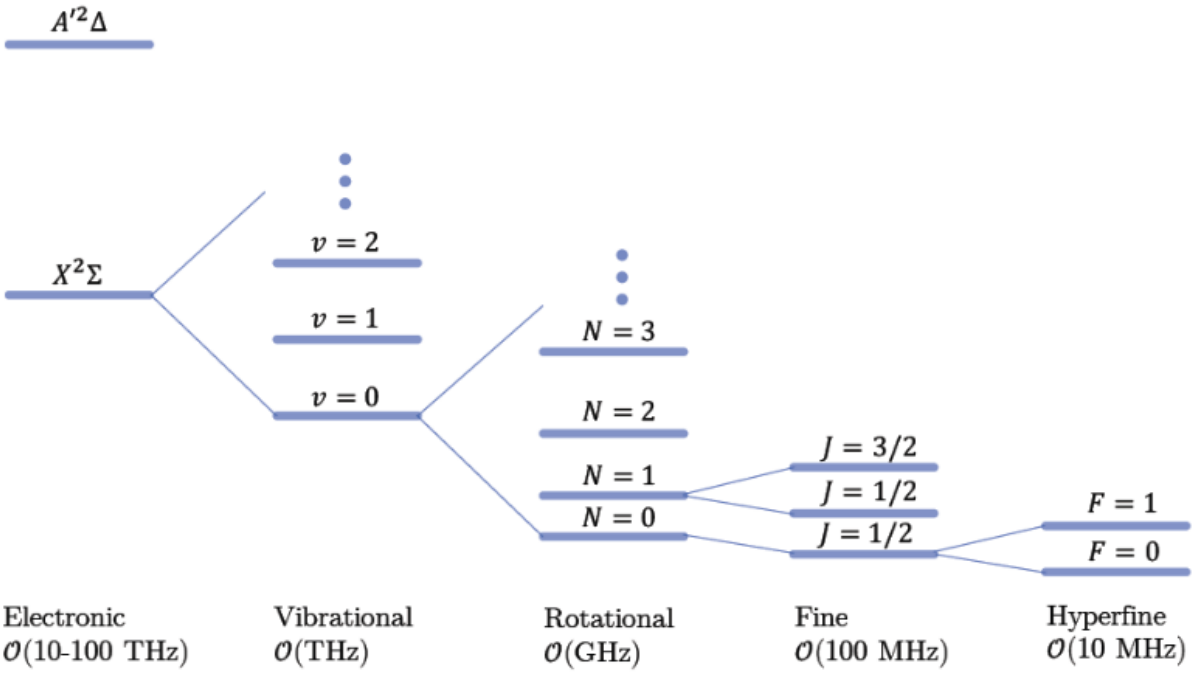

Figure 3: Adopted schematic from [12]. The molecular spectrum of BaF.

2.2 Detection & Measurement Principles

2.2.1 Signal to Noise Ratio

When both the signal (S) and the background (B) contributes to the noise, and the statistics of the detection follow Poisson distribution, the signal to noise formula [21] can be expressed:

$$SNR = \frac{S}{\sqrt{S+B}}, \tag{2}$$

as described for this experiment in [22, Chapter 3.3]. For the purpose of this thesis, the signal (S) is defined as the net signal, obtained by subtracting the background (B) from the total measured counts.

2.2.2 Experimental Sensitivity

The EDM can be interpreted solely in terms of d_e, the statistical uncertainty, including excessive noise, is given by:

$$\sigma_{d_e} = \frac{1}{W_d \mathcal{P}(E) T \sqrt{NM}}. \tag{3}$$

Where:

- σ_{d_e} is the statistical uncertainty on the electron electric dipole moment (eEDM),
- W_d is the effective electric field experienced by the electron within the molecule,
- $\mathcal{P}(E)$ is the electric field polarization factor (state preparation efficiency),
- T is the spin precession time,
- N is the number of detected molecules per pulse,
- M is the number of measurement pulses (shots),

The complete numerical analysis for this formula and the estimation of the current sensitivity calculation is available at: [12, Chapter 5.4].

2.3 Rabi Frequency and Excitation Dynamics

The interaction of atoms or molecules with electromagnetic radiation can be modeled using a two-level system, where the population oscillates coherently between a lower (ground) and an upper (excited) quantum state. When such a system is driven by a near-resonant monochromatic electric field, coherent population transfer occurs at a rate determined by the Rabi Frequency, which quantifies the coupling strength between the two states.

In the semiclassical treatment, the atom is described quantum mechanically, while the radiation field is treated classically. The total Hamiltonian is given by:

$$H = H_0 + H_I(t), \tag{4}$$

where H_0 is the unperturbed Hamiltonian of the atom, and $H_I(t)$ is the interaction Hamiltonian, given in the dipole approximation as:

$$H_I(t) = -\mathbf{d} \cdot \mathbf{E}(t), \tag{5}$$

with $\mathbf{d} = -e\mathbf{r}$ being the electric dipole operator, and $\mathbf{E}(t)$ the oscillating electric field:

$$\mathbf{E}(t) = \mathbf{E}_0 \cos(\omega t). \tag{6}$$

Applying the rotating wave approximation (RWA) and solving the time-dependent Schrödinger equation for the two-level system yields a key parameter, the *Rabi frequency*:

$$\Omega = \frac{eE_0 X_{12}}{\hbar}, \tag{7}$$

where $X_{12} = \langle 1|x|2\rangle$ is the matrix element of the dipole operator between the initial and final states. The Rabi frequency determines the rate at which population is coherently transferred between the two levels.
The electric field amplitude E_0 is related to the laser intensity I via $E_0 \propto \sqrt{I}$, so the Rabi frequency scales with the square root of intensity:

$$\Omega \propto \sqrt{I}. \tag{8}$$

When the laser is on resonance with the transition ($\omega = \omega_0$), the probability of finding the system in the excited state as a function of time becomes:

$$|c_2(t)|^2 = \sin^2\left(\frac{\Omega t}{2}\right), \tag{9}$$

indicating full population inversion when $\Omega t = \pi$.
More generally, including detuning $\Delta = \omega - \omega_0$, the excited-state population evolves as:

$$|c_2(t)|^2 = \frac{\Omega^2}{\Omega^2 + \Delta^2} \sin^2\left(\frac{1}{2}\sqrt{\Omega^2 + \Delta^2}\, t\right). \tag{10}$$

This coherent behavior is a signature of resonant excitation in a two-level system. The Rabi frequency is therefore central to understanding phenomena such as power broadening, saturation, and coherent control of population dynamics in atomic and molecular transitions.

2.4 Resonant Laser Induced Fluorescence (LiF)

The following mathematical derivation is adapted from [23, Chapters 7], which provides a detailed semiclassical treatment of atom–field interactions and two-level system excitations.

2.5 Power Broadening and Line Shape

When a two-level system is driven by an increasingly strong resonant laser field, the width of the transition line increases due to a phenomenon known as power broadening. This broadening arises from the saturation of the transition at high intensities, which alters the rate of absorption near resonance. The full width at half maximum (FWHM) of the Lorentzian component becomes:

$$\Delta\omega_{\mathrm{FWHM}} = \Gamma\left(1 + \frac{I}{I_{\mathrm{sat}}}\right)^{1/2}, \tag{11}$$

where Γ is the natural linewidth (the FWHM at low intensity), I is the applied laser intensity, and I_{sat} is the saturation intensity of the transition.

This expression describes the Lorentzian part of the spectral line, which is broadened by the increased Rabi frequency:

$$\Omega \propto \sqrt{I}. \tag{12}$$

The total line shape of an optical transition typically has a Voigt profile (see appendix B), which is a convolution of a Lorentzian and a Gaussian component. The Lorentzian component includes natural and power broadening effects, while the Gaussian component primarily arises from Doppler broadening due to the motion of atoms or molecules.

2.5.1 Intensity Saturation

In a two-level system driven by resonant electromagnetic radiation, the absorption rate initially increases linearly with intensity. However, as the intensity becomes comparable to a characteristic value known as the saturation intensity, the absorption begins to level off and eventually saturates.
The saturation intensity I_{sat} is defined as the intensity at which the excited-state population reaches half of its maximum value under continuous wave excitation. For a closed two-level system, it is given by:

$$I_{\text{sat}} = \frac{\pi hc\Gamma}{3\lambda^3}, \tag{13}$$

where:

- Γ is the natural linewidth (spontaneous decay rate),
- λ is the transition wavelength,
- h is Planck's constant,
- c is the speed of light.

Here, Γ is the natural linewidth (spontaneous decay rate), which itself depends on the excited state lifetime τ as

$$\Gamma = \frac{1}{\tau} \tag{14}$$

This defines how quickly the population decays from the excited state. The corresponding linewidth in frequency units (Hz), known as the full width at half maximum (FWHM), is:

$$\Delta\nu = \frac{\Gamma}{2\pi} = \frac{1}{2\pi\tau} \tag{15}$$

These relationships are critical when interpreting spectral features or estimating saturation effects, as they directly tie the natural broadening of a transition to its temporal dynamics.

The steady-state population of the excited state is then given by:

$$\rho = \frac{1}{2} \cdot \frac{I/I_{\text{sat}}}{1 + I/I_{\text{sat}}}, \tag{16}$$

which shows that:

- At low intensity ($I \ll I_{\text{sat}}$), $\rho \propto I$, i.e., absorption grows linearly.
- At high intensity ($I \gg I_{\text{sat}}$), $\rho \to \frac{1}{2}$, i.e., the population saturates, and further increasing intensity does not enhance excitation efficiency.

This behavior is reflected in both the signal intensity and the absorption cross-section:

$$\sigma(\omega, I) = \frac{\sigma_0}{1 + I/I_{\text{sat}}}, \tag{17}$$

where σ_0 is the peak absorption cross-section at low intensity. Thus, saturation leads to a reduction in effective absorption and contributes to power broadening of the Lorentzian line profile.
In molecular systems such as the $X^2\Sigma^+ \to D^2\Sigma^+$ excitation, saturation effects must be accounted for when interpreting fluorescence signals, as the response will deviate from a purely linear intensity dependence at high powers.

3 Experimental Setup

3.1 Experimental setup of NL-eEDM

The experimental setup of the NL-eEDM collaboration is shown in Figure 4.

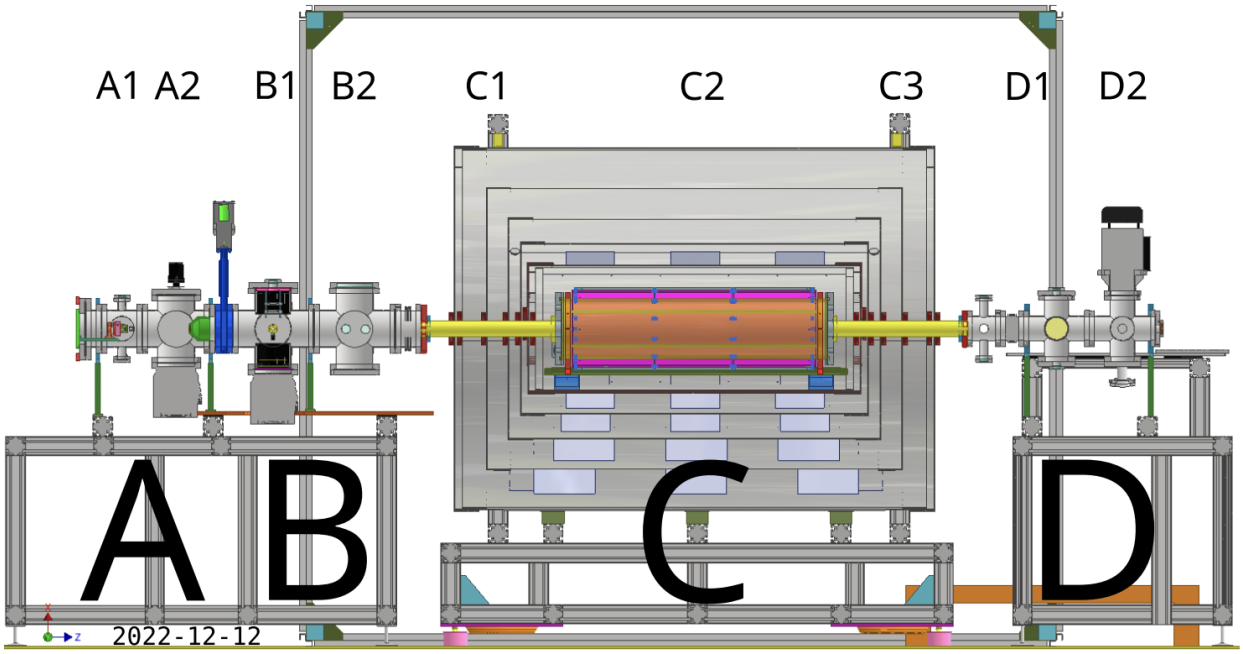

Figure 4: The molecular beam propagates from left to right through four main sections labeled **A** to **D**. Section **A** represents the cryogenic source from which barium monofluoride BaF molecules are emitted, then collimated and cooled. In section **B**, the molecular state preparation zone is shown. In **B1**, the initial detection of the molecules is performed using photomultiplier tubes (PMTs). Section **B2** is the most relevant for this thesis, as it is where the excitation of from the ground state is implemented to prepare the desired quantum state of the molecules. The central part of the experiment is the interaction zone at section **C**, in which the spin precession occurs under the influence of electric and magnetic fields. The BaF molecules end up in section **D**, where final state detection takes place. Here, additional PMTs detect fluorescence, and counter-propagating laser beams are used to drive the two-photon transition required for readout [24].

The relevant sections of the experimental setup for this thesis are as follows:
In *section A*, where the the supersonic beam source is located. This source emits a beam of barium monofluorine BaF molecules, which are subsequently collimated and cooled.

In *section B1*, the excitation of the molecules is performed using a probe laser. *Section B2* serves as the normalization region. Due to the large pulse-to-pulse fluctuations in the number of molecules emitted by the source, B2 provides a reference signal used to normalize the fluorescence measurements, thus improving the accuracy of the results (see Section 3.3).

Finally, in *Section D2*, the laser-induced fluorescence (LIF) detection is carried out using a counter-propagating laser beam. The resulting fluorescence is collected by photomultiplier tubes (PMTs), allowing for state-selective readout of the excited molecular population.

3.2 Experimental Setup of the Laser

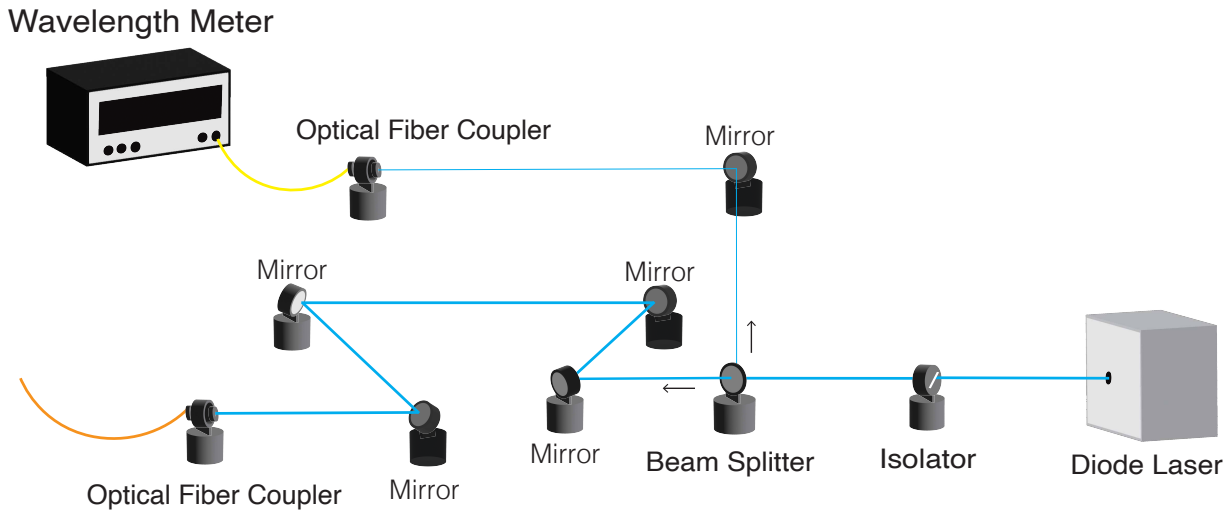

Figure 5: Schematic of the optical setup for the blue laser system. The laser beam, emitted from the diode laser (bottom right), first passes through an optical isolator to suppress back-reflections that could destabilize the laser output. It is then directed into a beam splitter. Approximately 10% of the beam is reflected and guided towards a power meter for real-time monitoring, while the remaining 90% is transmitted through the beam splitter. This transmitted beam is guided by a sequence of mirrors and coupled into an optical fiber, which delivers the beam to the experiment region. (A picture of the laser taken from the Lab can be seen in appendix C).

3.3 Laser Setup Coupling to the Experimental Setup

The laser beam, after being fiber-coupled to the *orange optical fiber*, is directed onto a sequence of mirrors that align it with the molecular beamline. Figure 6 show the final section of the optical path, where the beam is focused through an aperture and slit before entering the interaction zone of the NL-eEDM experiment. This alignment is crucial to ensure that the laser properly overlaps with the BaF molecular beam. The probe laser as shown in Figure 6.B, it is orthogonal to the molecular beam, resulting in approximately Doppler free detection.

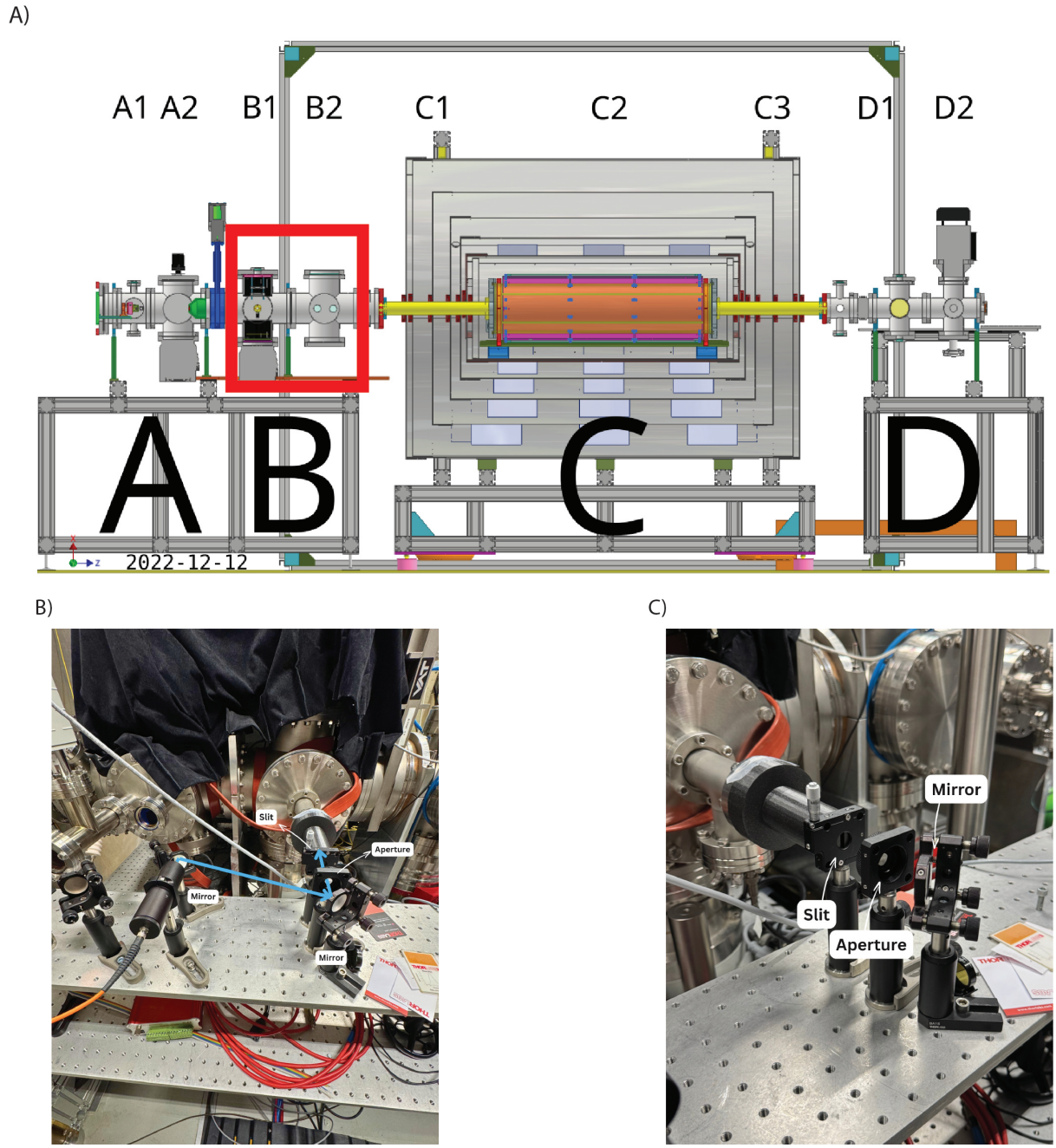

Figure 6: **(A)** Schematic of the full NL-eEDM setup, with the red box highlighting the region where the laser beam is coupled into Figure 4. **(B)** View of the final section of the optical path, where the laser beam is coupled to (red box). **(C)** Close-up of the aperture and slit through which the laser is probed inside the experimental setup.

3.4 Characterization of the Laser Beam Profile

To evaluate the spatial properties of the blue laser used in this experiment, the output beam was inspected visually and measured using a beam profiler. A clear multimode structure was observed, as shown in Figure 8.

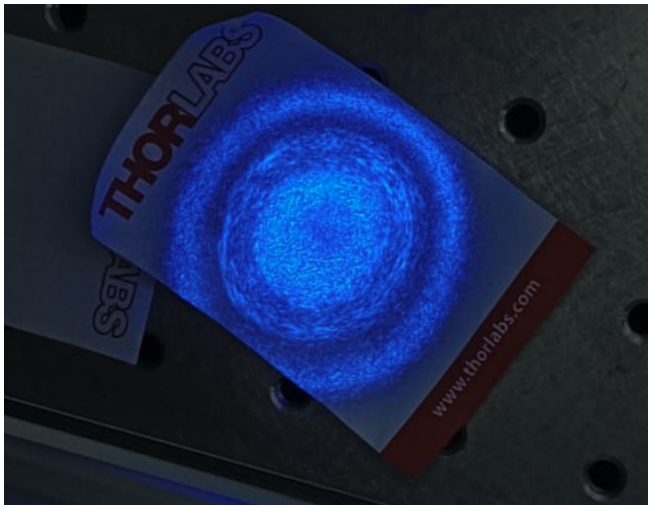

Figure 7: Laser beam projection on a beam viewing card. The diameter of the laser beam is measured at ≈ 1 cm.

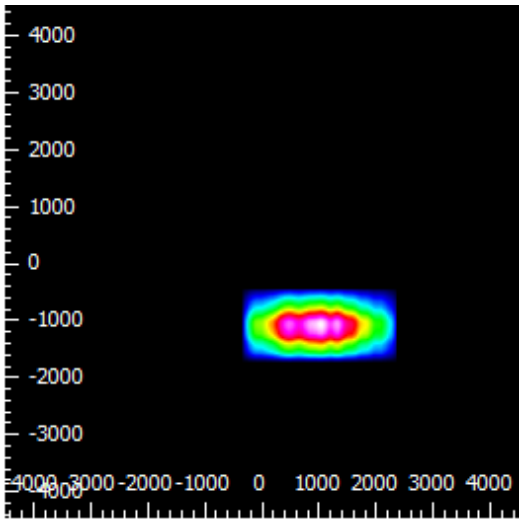

Figure 8: Characterization of the laser beam at the diode output.This images indicate that the laser operates in a multimode regime. Meaning that it is not Gaussian shaped and not spatially coherent.

4 Methods

4.1 Locating the Resonant Transition

The biggest challenge using this blue laser was to experimentally determine the frequency corresponding to the targeted transition ($X^2\Sigma^+$ to $D^2\Sigma^+$). Theoretical estimates were provided via private communication with members of the NL-eEDM theory group at the University of Groningen. A frequency value for the ($X^2\Sigma^+$ to $D^2\Sigma^+$) is given in [25, Chapter 3.4] corresponding to a value of 724795734 MHz. Some theoretical calculations can can be found also in [26].

Firstly, the laser diode used in this laser setup was installed inside a protective metal housing. The laser beam exited the housing through a small optical aperture and was directed onto the optical table for collimation and alignment. Although the diode was enclosed inside the metal housing, its output can be seen through the beam path (see Section 3.2). The resulting laser beam was then reflected through a sequence of mirrors and was directed onto a beam splitter. After the beam splitter, 90% of the laser beam was coupled through a sequence of mirrors to an optical fiber, in order to be delivered to the experiment region as seen in Section 3.3 . The remaining 10% of the laser beam was directed to a wavelength meter to ensure that the laser remains in a single, well-defined stable frequency mode. As discussed in [27], a stable laser mode ensures that laser noise, including frequency drifts and intensity fluctuations, won't negatively impact the laser performance.

Once the setup was complete, the mirrors were carefully adjusted, so the maximum laser power is delivered into both optical fibers. The laser power itself is controlled via a electric current controller, which allows precise adjustments of the current (I) supplied to the diode.

The following description of the transition search procedure and frequency determination is based on internal lab notes written by Bastiaan Nijman (May 2025):

The first successful measurement for the ($X^2\Sigma^+$ to $D^2\Sigma^+$) transition was recorded on May 23, 2025. For reproducibility purpose, the exact values are given: The laser was set to a current of $I = 39.59\,\mathrm{mA}$ and a temperature setting of 31.7°C (measured 31.6°C). The optical power just before the fiber was measured at 6.07 mW.

In order to search for this transition, an external oscillator was connected to the laser to modulate its current and enable frequency scanning. The scan rate was set to about 1 MHz/s as there are 10 shots of molecule per second.

During the scan, signals were observed at higher frequencies, specifically from 739.942 to 739.946 THz. A narrow signal structure appeared around 739.9461THz, prompting a finer scan in this region. Eventually, a strong signal was clearly identified at approximately 739.946 THz. This value was about 2.5 GHz higher than the original theoretical estimate, suggesting the transition observed could be associated with a $N = 3 \rightarrow N' = 4$ rotational branch within the $D^2\Sigma^+$ manifold.

5 Results

5.1 Identification of the Resonant Transition

Following the transition search procedure described in Section 4, the measured resonance laser induced fluorescence (LIF) spectrum for the $X^2\Sigma^+(N=0) \rightarrow D^2\Sigma^+(N=1)$ transition with their accompanied errors are shown in Figure 9. This spectrum corresponds to a laser configuration with the following parameters:

Parameter	**Description**
Laser Frequency	739.94638 THz
Laser Power (before the aperture)	3.4 mW
Laser Power (after slit)	0.8 mW
Beam Delivery Method	Multimode optical fiber
Beam Profile	Broad, multimode output with non-Gaussian distribution
Aperture Radius	$\approx$ 1 cm before slit (Figure 7) : effective spot size unknown after fiber
Intensity Estimation	$\approx$ 1 mW/cm^2 but not precisely calculated due to large spot size (Figure 7) and multimode fiber structure(Figure 8)

Table 2: Experimental parameters relevant for the measured transition spectrum shown in Figure 9. These parameters reflect the configuration during which the laser frequency was recorded.

Figure 7 illustrates the laser beam emerging from the optical fiber. A diameter of about 1 cm was measured for this particular beam spot projected onto the beam card. The area of this beam is given by: $A = \pi \cdot r^2$, which results in approximately 0.785 cm^2. This value provides an upper bound on the illuminated region before entering the aperture and slit (as depicted in Figure 6). From Figure 8, the beam profiler appears non-Gaussian, as expected for a multi-mode fiber. This further complicates precise intensity estimation, especially after the slit, where the effective beam spot size is difficult to be measured.

Despite these limitations, the power measured after the slit was $P = 0.8$ mW, which combined with the approximate area of the beam after the slit, yields an estimate for the given intensity of the laser: $I \approx 1$ mW/cm^2. However, taking into consideration the use of a multi-mode fiber and the width of the beam, it becomes evident that any estimation of the intensity would be highly uncertain and not meaningful. As a result the intensity cannot be reliably extracted from the measurements. For this reason and for the rest of this analysis, only the laser power $P = 0.8$ mW will be considered as the relevant quantity.

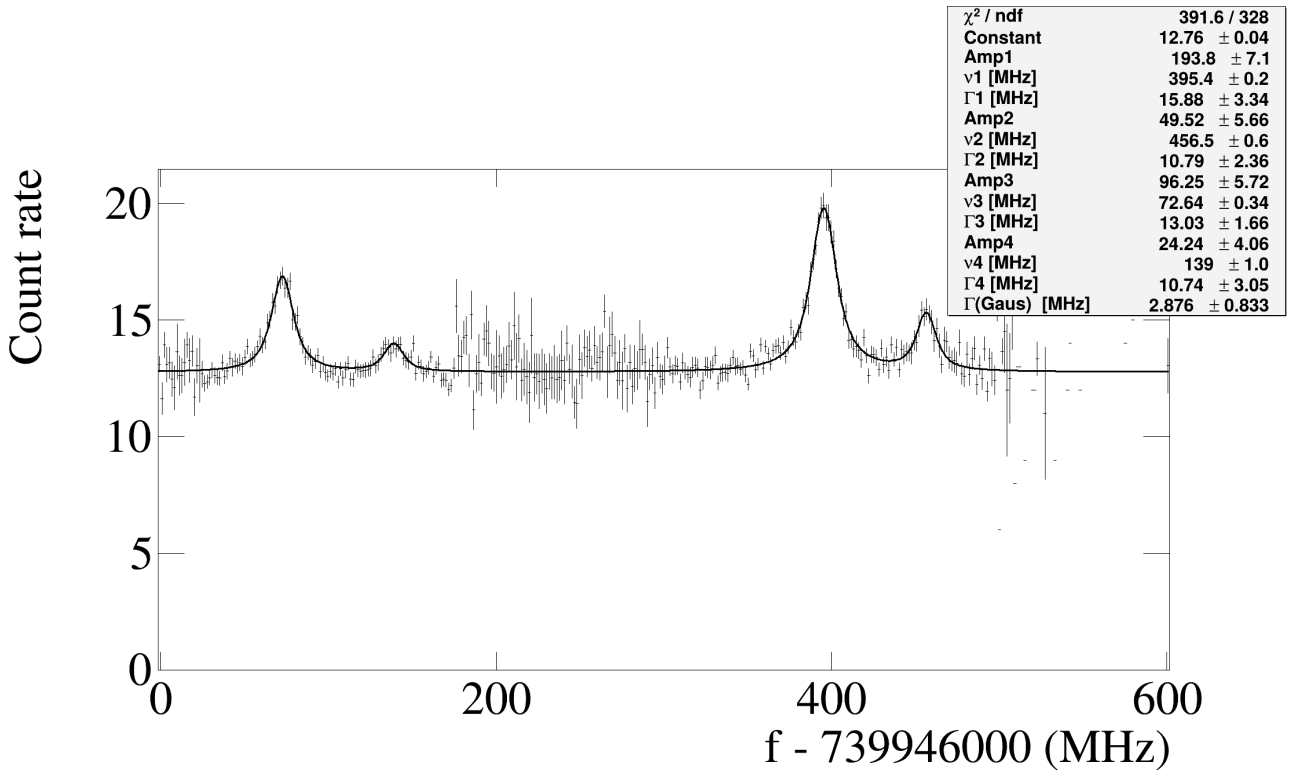

Figure 9: The measured resonance laser induced fluorescence (LIF) spectrum for the $X^2\Sigma^+(N=0) \rightarrow D^2\Sigma^+(N=1)$ transition at P = 0.8 mW

Parameter	**Value**	**Uncertainty**
χ^2/ndf	391.6 / 328	–
Constant	12.76	± 0.04
Amp1	193.8	± 7.1
ν_1 [MHz]	395.4	± 0.2
Γ_1 [MHz]	15.88	± 3.34
Amp2	49.52	± 5.66
ν_2 [MHz]	456.5	± 0.6
Γ_2 [MHz]	10.79	± 2.36
Amp3	96.25	± 5.72
ν_3 [MHz]	72.64	± 0.34
Γ_3 [MHz]	13.03	± 1.66
Amp4	24.24	± 4.06
ν_4 [MHz]	139	± 1.0
Γ_4 [MHz]	10.74	± 3.05
Γ_{Gaus} [MHz]	2.876	± 0.833

Table 3: Fit parameters extracted from the Voigt profile fitting of the resonance spectrum.

5.2 Experimental Verification of the Resonant Transition

In Section 4, theoretical expectations for the $X^2\Sigma^+(N=0) \rightarrow D^2\Sigma^+(N=1)$ transitions were outlined. Given the measured spectrum in Figure 9, a comparison with these expectations provides a useful consistency check, before proceeding with a detailed analysis of the spectral features in Section 5.3.

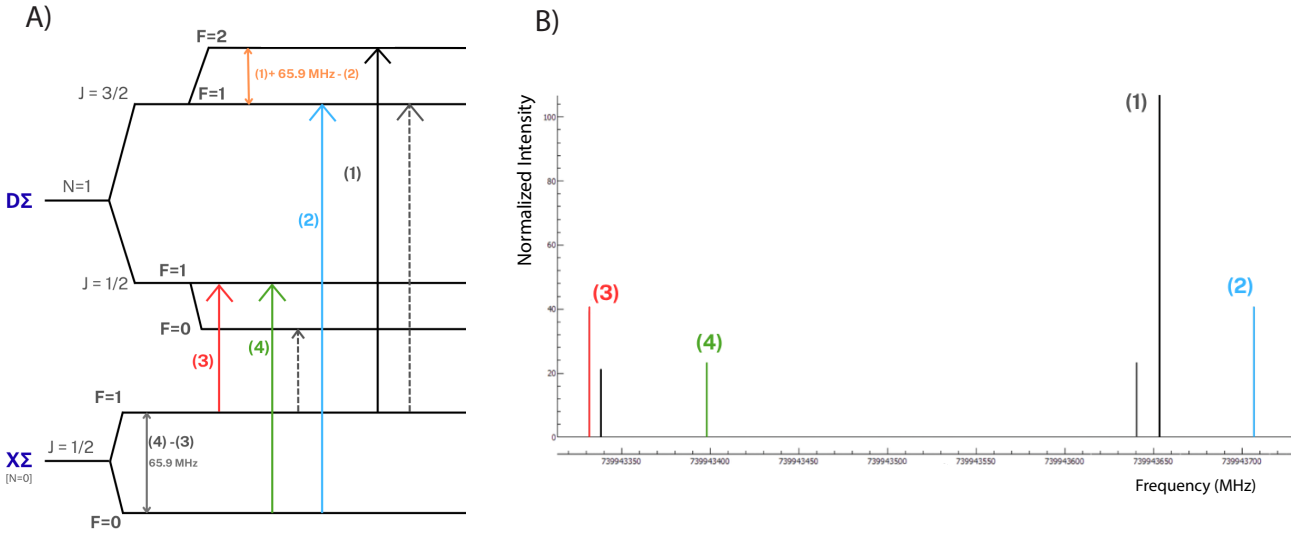

Figure 10: Schematic 9**A** illustrates the relevant hyperfine structure of the BaF for the $X^2\Sigma^+(N=0) \rightarrow D^2\Sigma^+(N=1)$ transition. The dashed lines represent the suppressed transitions. Figure 9**B** presents the corresponding expected fluorescence spectrum, featuring the predicted peak positions associated with the labeled transitions. Spectrum predicted by [28, PGopher] with molecular parameters given in [25].

The six peaks expected in the laser induced fluorescence spectrum correspond to six possible hyperfine transitions between $X^2\Sigma^+(N=0)$ and $D^2\Sigma^+(N=1)$ states, including two transitions which are weakly allowed or suppressed. These transition are only a few MHz away from the other allowed transitions and for that reason are not labeled in Figure 10. Since the energy differences between hyperfine levels translate directly into frequency differences via $E = h\nu$, the relative frequency spacing between the peaks can be used in order to relate the transitions from Figure 10A with their peaks from Figure 10B.

Among these six transition, the one with the highest predicted fluorescence intensity corresponds to the $F = 1 \rightarrow F = 2$ excitation from the $X^2\Sigma^+(N=0)$ to the $D^2\Sigma^+(N=1)$ excited state. The hyperfine splitting of the ground state is expected at 65.9 MHz.

In order to facilitate a comparison between theoretical expectations and experimental observations, an overlay of Figure 10 and Figure 9 was created, that is Figure 11. The overlay between these two plots, allows for a visual comparison of the predicted frequencies and the measured peak positions. However, since no explicit theoretical value for the absolute transition frequency is provided, no numerical comparison between the experimental frequency and a theoretical reference is made. The experimental frequency is 739.94638 THz, as stated in the data from Table 2.

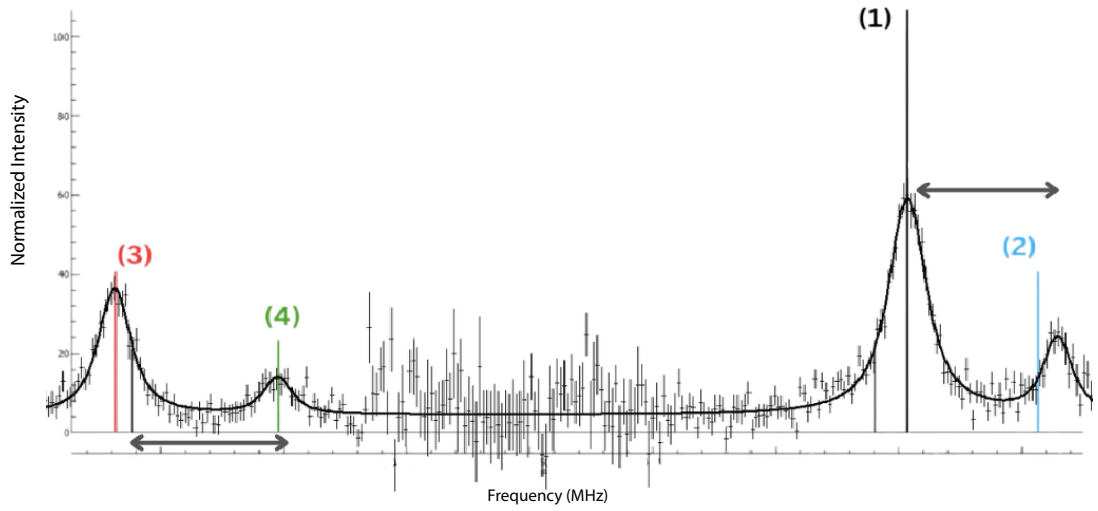

Figure 11: Overlay between the measured fluorescence and the theoretical expectations for the $X^2\Sigma^+(N=0) \rightarrow D^2\Sigma^+(N=1)$ transition in BaF. The labeled peaks correspond to hyperfine resolved transitions, with the predicted position imposed on the experimental data. The numerical values shown on the graph indicate experimentally extracted frequency differences between selected peaks.

In Figure 11, only four distinct peaks are observed. However, due to the resolution limitations of the current PMTs, and the broader linewidths of the dominant transitions, the two weekly allowed excitations seem to be embedded within the broader peaks and cannot be individually resolved.

The frequency difference between peak (3) and peak (4) is associated with the hyperfine splitting of the ground state $X^2\Sigma^+$. The theoretical value for this splitting is 65.9 MHz. The experimental value, calculated by subtracting ν_3 from ν_4 in Table 2, yields 66.4 ± 1.1 MHz, which is consistent with the expected value within the experimental uncertainty.

Similarly, the frequency difference between peak (2) and peak (1) is calculated: 61.1 ± 0.6 MHz, which also falls within a reasonable range. A predicted value of 50 MHz is given by Figure 10**B**.

The difference in the hyperfine splitting $F = 1$ and $F = 2$ for the excited state $D^2\Sigma^+(N=1)$ can be calculated by taking the difference between the two previously extracted splittings. In Figure 10, this difference is illustrated in orange color. This splitting is calculated at: $\Delta\nu = 5.3 \pm 1.3$ MHz.

The following Table 4 is a numerical summary of Section 5.2:

Quantity	**Experimental Value**	**Theoretical Value**	**Notes**
$\nu_4 - \nu_3$ (Ground state $X^2\Sigma^+$ splitting)	66.4 ± 1.1 MHz	65.9 MHz	Consistent with theory
$\nu_1 - \nu_2$ (Upper peak spacing)	61.1 ± 0.6 MHz	–	Within reasonable range. Prediction (Figure 10**B**) is 50 MHz
$\Delta\nu = (\nu_4 - \nu_3) - (\nu_1 - \nu_2)$	5.3 ± 1.3 MHz	–	Difference in excited state splitting (orange arrow)

Table 4: Summary of measured frequency splittings and comparisons with theoretical expectations for the BaF hyperfine transitions.

5.3 Quantitative Analysis of the Laser Induced Fluorescence (LIF) Signal

In Section 5.1 , the parameters to required to observe the desired transition experimentally were determined. In Section 5.2, a comparison between the measured spectrum and theoretical predictions, as provided through private communication with members of the NL-eEDM theory group at the University of Groningen was performed. The last part of the Results section provides a quantitative analysis of the observed data and their relevance to the detection scheme performance.

From the measured spectrum in Figure 9, the signal peak rises to approximately 7 counts above the background signal of 13 counts. The Gaussian component of the Voigt fit, associated with Doppler broadening, yields a value at full width half maximum (FWHM) of 2.88 ± 0.84 MHz. As mentioned in Figure 6, the probe laser is perpendicular to the molecular beam, which ideally results in Doppler free detection. As a consequence, the Gaussian should be constant for all the measurements. However, some residual Doppler broadening remains observable.

The natural linewidth was calculated theoretically using Equations (14) and (15), based on a predicted excited state lifetime of 39.1 ns (private communication, NL-eEDM theory group). This results in a natural linewidth value of approximately 5 MHz.

Due to limited available laser power and the current beam configuration, which consists of a broad multi-mode output laser beam, it was not possible to perform a power broadening measurement to experimentally determine the saturation intensity. As a result the saturation intensity was estimated using theoretical considerations (Equation (13)). This theoretical value is calculated: $I_{sat} \approx 10\ mW/cm^2$.

Note: Preliminary data were also collected for the additional rotational (N) transition. However, these transitions were not analyzed in depth. The recorded spectra of such transitions can be found in appendix D, but are not relevant for this thesis and therefore not discussed further.

6 Discussion

This work presents the first experimental observation of the $X^2\Sigma^+(N=0) \rightarrow D^2\Sigma^+(N=1)$ transition in barium monofluorine BaF, marking a significant milestone towards the spectroscopic study of the BaF molecule. Theoretical predictions were confirmed, and laser induced fluorescence spectra were obtained with hyperfine resolved excitation.

Despite this achievement, several limitations constrained the full characterization of this transition, particularly limitations related to the laser configuration. One of the primary challenges was the limited available laser power and the broad multimode output of the laser beam. These factors significantly reduced the laser intensity at the interaction zone of the NL-eEDM experiment. As a consequence, measurements were restricted to a single laser power value of 0.8 mW, as measured after the slit. With increased available power and a single-mode laser beam profile, the saturation intensity could be determined by increasing the laser intensity until the fluorescence signal reaches a plateau and no longer increases with additional power.

It is recommended to install a new PMT filter to further reduce the background signal. The low signal to noise ratio (SNR), evident in a modest signal of about 7 counts above the background, limited the sensitivity of the measurements. The current PMTs, with 8% Quantum Efficiency and solid angle coverage of 2%, also leave room for improvement in the collection efficiency.

In addition to these detection limitations, the current setup allows for a reliable experimental verification of the expected branching ratios from the $D^2\Sigma^+$ state. These branching ratios are essential for validating the theoretical model and addressing an important aspect of this new detection scheme: whether a significant fraction of spontaneous decay occurs to the $A^2\Pi$ state, or if other states may be more favorable for detection. Future work could address this by employing a depletion test, in which population loss is monitored.

Another crucial factor was the fluctuations in molecular flux because of the pulse to pulse variation from the supersonic beam source, which directly impacted the collected signal strength above background. The maximum number of detected counts, achieved under optimized alignment and increased molecule production, was at around 80 counts for the same power of 0.8 mW. This value contrasts sharply with the typical signal of about 7 counts above background observed in the experimental data, highlighting the significance of maximizing and stabilizing the number of molecules produced.

It is observed that, although the probe laser was ideally perpendicular to the molecular beam, residual Doppler broadening appeared in the Gaussian component of Voigt profile fits, suggesting minor beam misalignment or molecular velocity spread, as expected. This underscores the importance of precise beam overlap and alignment for the NL-eEDM setup

Due to the limited signal strength and all the different limitations mentioned, a quantitative comparison between the proposed and previous detection scheme could not be performed. As a result, key hypotheses, such as the background free detection could not yet be experimentally verified. Nevertheless, with improved experimental conditions, particularly regarding laser intensity and beam quality, the proposed approach seems promising for high precision and future applications in the BaF NL-eEDM experiment.

7 Conclusion

This thesis successfully presents the first experimental observation of the $X^2\Sigma^+(N=0) \rightarrow D^2\Sigma^+(N=1)$ transition in barium monofluorine BaF, achieving hyperfine-resolved laser-induced fluorescence and confirming theoretical predictions. This result marks a significant step towards the comprehensive spectroscopic investigation of BaF, with particular relevance to the precision measurement in the NL-eEDM.

Despite this success, several experimental limitations, such as low power, multimode beam profile, limited photon collection efficiency and fluctuation in the molecular flux, constrained the ability to fully characterize this new detection scheme. These factors prevented the measurement of saturation intensity and hindered a quantitative comparison with the previously used detection scheme.

Nonetheless, the successful observation of this transition under challenging conditions demonstrates the feasibility of using this scheme for future high precision spectroscopic work in BaF. With targeted improvements, this method seems promising for advancing the detection capabilities required in the NL-eEDM experiment.

7.1 Future Outlook

In future work, efforts should initially focus on increasing laser power and implementing a single-mode beam profile. Improving detection efficiency via enhanced PMTs and optimized alignment is not specific to this detection scheme but remains an essential area for continuous improvement. Additionally, a depletion test and further analysis of the decay branching ratios from the $D^2\Sigma^+$ state would provide valuable insight for this detection scheme. These developments would enable a full quantitative comparison with the existing detection schemes as stated in the Hypothesis.

Bibliography

[1] E. M. Purcell and N. F. Ramsey, "On the possibility of electric dipole moments for elementary particles and nuclei," *Physical Review*, vol. 78, p. 807, June 1950. https://doi.org/10.1103/PhysRev.78.807.

[2] T. D. Lee and C. N. Yang, "Question of parity conservation in weak interactions," *Physical Review*, vol. 104, pp. 254–258, Oct. 1956. https://doi.org/10.1103/PhysRev.104.254.

[3] J. H. Smith, E. M. Purcell, and N. F. Ramsey, "Experimental limit to the electric dipole moment of the neutron," *Physical Review*, vol. 108, pp. 120–122, Oct. 1957. https://doi.org/10.1103/PhysRev.108.120.

[4] C. J. Ho, J. A. Devlin, I. M. Rabey, P. Yzombard, J. Lim, S. C. Wright, N. J. Fitch, E. A. Hinds, M. R. Tarbutt, and B. E. Sauer, "New techniques for a measurement of the electron's electric dipole moment," *New Journal of Physics*, vol. 22, p. 053031, May 2020. https://doi.org/10.1088/1367-2630/ab83d2.

[5] I. B. Khriplovich and S. K. Lamoreaux, *CP Violation Without Strangeness: Electric Dipole Moments of Particles, Atoms, and Molecules*. Berlin, Heidelberg: Springer-Verlag, 1997.

[6] Y. Ema, T. Gao, and M. Pospelov, "Standard model prediction for paramagnetic electric dipole moments," *Physical Review Letters*, vol. 129, p. 231801, Nov. 2022. https://doi.org/10.1103/PhysRevLett.129.231801.

[7] E. for the 2π Decay of the K_2^0 Meson, "Evidence for the 2π decay of the k_2^0 meson," *Physical Review Letters*, vol. 13, pp. 138–140, July 1964. https://doi.org/10.1103/PhysRevLett.13.138.

[8] Y. Hao, *Theoretical Investigations for Testing the Fundamental Symmetries of the Standard Model with Diatomic Molecules*. Phd thesis, University of Groningen, Groningen, The Netherlands, 2020. https://doi.org/10.33612/diss.127488441.

[9] T. S. Roussy, L. Caldwell, T. Wright, W. B. Cairncross, Y. Shagam, K. B. Ng, N. Schlossberger, S. Y. Park, A. Wang, and E. A. Cornell, "An improved bound on the electron's electric dipole moment," *Science*, vol. 381, pp. 46–50, July 2023. http://dx.doi.org/10.1126/science.adg4084.

[10] M. Pospelov and A. Ritz, "Electric dipole moments as probes of new physics," *Annals of Physics*, vol. 318, pp. 119–169, July 2005. https://doi.org/10.1016/j.aop.2005.04.002.

[11] P. Aggarwal, H. L. Bethlem, A. Borschevsky, M. Denis, K. Esajas, P. A. B. Haase, Y. Hao, S. Hoekstra, K. Jungmann, T. B. Meijknecht, M. C. Mooij, R. G. E. Timmermans, W. Ubachs, L. Willmann, and A. Zapara, "Measuring the electric dipole moment of the electron in baf," *European Physical Journal D*, vol. 72, Nov. 2018. https://doi.org/10.1140/epjd/e2018-90192-9.

[12] A. Boeschoten, *Precision Measurements in Diatomic Molecules: a Route to a Permanent Electric Dipole Moment*. Phd thesis, University of Groningen, Groningen, The Netherlands, 2023. https://doi.org/10.33612/diss.674231809.

[13] V. R. Marshall, *Spectroscopy and Systematic Effects: an eEDM experiment using BaF molecules*. Phd thesis, University of Groningen, Groningen, The Netherlands, 2024. https://doi.org/10.33612/diss.972290628.

[14] P. Aggarwal, V. R. Marshall, H. L. Bethlem, A. Boeschoten, A. Borschevsky, M. Denis, K. Esajas, Y. Hao, S. Hoekstra, K. Jungmann, T. B. Meijknecht, M. C. Mooij, R. G. E. Timmermans, A. Touwen, W. Ubachs, S. M. Vermeulen, L. Willmann, Y. Yin, and A. Zapara, "Lifetime measurements of the $a\ ^2\Pi_{1/2}$ and $a\ ^2\Pi_{3/2}$ states in baf," *Physical Review A*, vol. 100, p. 052503, Nov. 2019. https://doi.org/10.1103/PhysRevA.100.052503.

[15] V. K. Sumbre, *Improving the Signal Readout of an eEDM Experiment*. Bachelor thesis, University of Groningen, July 2023.

[16] T. Tiemens, *Investigating the Viability of Using Avalanche Photodiodes for State Detection of BaF in the NL-eEDM Experiment*. Bachelor thesis, University of Groningen, July 2022.

[17] Hamamatsu Photonics K.K. Editorial Committee, *Photomultiplier Tubes: Basics and Applications*. Japan: Hamamatsu Photonics K.K., Electron Tube Division, 4th ed., 2017.

[18] S. V. Polyakov, "Photomultiplier tubes," in *Handbook of Photon Detection*, ch. 3, pp. 69–82, Gaithersburg, MD, USA: National Institute of Standards and Technology (NIST), 2022.

[19] A. Touwen, *Readout and control of molecules for electric dipole moment searches*. Phd thesis, University of Groningen, Groningen, The Netherlands, 2024. https://doi.org/10.33612/diss.1106847702.

[20] P. K. Mallick, *Fundamentals of Molecular Spectroscopy*. Singapore: Springer Nature Singapore, 1st ed., 2023.

[21] Hamamatsu Photonics K.K. Editorial Committee, *Photomultiplier Tubes: Basics and Applications*. Hamamatsu Photonics K.K., Electron Tube Division, 3rd ed., 2007.

[22] E. B. Blyumin, *Counting Statistics of an Electron Electric Dipole Moment Experiment*. Bachelor thesis, University of Groningen, Apr. 2023.

[23] C. J. Foot, *Atomic Physics*. Oxford, United Kingdom: Oxford University Press, 1st ed., 2005.

[24] T. B. Meijknecht, *Electric and Magnetic Field Control for Electric Dipole Moment Searches*. Phd thesis, University of Groningen, Groningen, The Netherlands, 2023. https://doi.org/10.33612/diss.822567899.

[25] M. C. Mooij, *A Cryogenic Buffer Gas Beam Source of BaF Molecules*. Phd thesis, Vrije Universiteit Amsterdam, Amsterdam, The Netherlands, June 2025. https://doi.org/10.5463/thesis.1236.

[26] C. Effantin, A. Bernard, J. d'Incan, G. Wannous, J. Vergès, and R. F. Barrow, "Studies of the electronic states of the baf molecule," *Molecular Physics*, vol. 70, no. 5, pp. 735–745, 1990. https://doi.org/10.1080/00268979000101311.

[27] R. Paschotta, "Stabilization of lasers." RP Photonics Encyclopedia, 2005. Available online at https://www.rp-photonics.com/stabilization_of_lasers.html.

[28] C. M. Western, "Pgopher: A program for simulating rotational, vibrational and electronic spectra," *Journal of Quantitative Spectroscopy and Radiative Transfer*, vol. 186, pp. 221–242, Jan. 2017. https://doi.org/10.1016/j.jqsrt.2016.04.010.

Appendices

A Python Script for visualizing the data

Listing 1: The seaborn library is used for data visualisation of the measurements

```
# Install seaborn library
!pip install seaborn

# Import libraries
import matplotlib.pyplot as plt
import numpy as np
import seaborn as sns
from google.colab import files

# Upload both files (manual file picker)
uploaded = files.upload()

# Define function to read float values
def read_numbers(filename):
    with open(filename, 'r') as file:
        return [float(line.strip()) for line in file]

# Load data from files
numbers1 = read_numbers('I_High.txt')
numbers2 = read_numbers('I_High_Frequency.txt')
print("Loaded", len(numbers1), "values from I_High.txt")
print("Loaded", len(numbers2), "values from I_High_Frequency.txt")

# Define frequency range of interest
lower_bound = 739.94636
upper_bound = 739.94641

# Filter values within this frequency range
filtered = [(x, y) for x, y in zip(numbers1, numbers2)
           if lower_bound <= y <= upper_bound]

# Separate into counts and frequency lists
filtered_freq = [y for x, y in filtered]
filtered_counts = [x for x, y in filtered]

# Scatter plot
plt.figure(figsize=(10, 6))
plt.scatter(filtered_freq, filtered_counts, s=10, color='black', marker='s')
plt.title('Photon Counts vs Frequency')
plt.xlabel('Frequency (THz)')
plt.ylabel('Photon Counts')
plt.grid(True)
plt.show()

# Binned seaborn plot (no regression)
sns.regplot(x=filtered_freq, y=filtered_counts, x_bins=30, fit_reg=False)

# Fix x-axis limits for consistency
center = (lower_bound + upper_bound) / 2
span = upper_bound - lower_bound
```

```
plt.xlim(center - span / 2, center + span / 2)

plt.title('Photon Counts vs Frequency')
plt.xlabel('Frequency (THz)')
plt.ylabel('Photon Counts')
plt.grid(True)
plt.tight_layout()
plt.show()
```

B Voigt Profile Analysis

The Voigt profile is represented as the convolution of a Lorentzian and a Gaussian:

$$y = y_0 + \int_{-\infty}^{\infty} (f_1 \cdot f_2)\, dx$$

where:

$$f_1(x) = \frac{2A}{\pi} \cdot \frac{w_L}{4(x - x_c)^2 + w_L^2}$$

and

$$f_2(x) = \sqrt{\frac{4\ln 2}{\pi}} \cdot \frac{e^{-\frac{4\ln 2 \cdot x^2}{w_G^2}}}{w_G}$$

are the Lorentzian and Gaussian respectively. The Voigt profile is given by:

$$y = y_0 + \frac{2A\ln 2}{\pi^{3/2}} \cdot \frac{w_L}{w_G^2} \int_{-\infty}^{\infty} \frac{e^{-t^2}}{\left(\sqrt{\ln 2} \cdot \frac{w_L}{w_G}\right)^2 + \left(\sqrt{4\ln 2} \cdot \frac{x - x_c}{w_G} - t\right)^2} dt$$

And the full width at half maximum (FWHM) for a Voigt profile can be approximated as:

$$\text{FWHM} = 0.5346 \cdot w_L + \sqrt{0.2166 \cdot w_L^2 + w_G^2}$$

, where w_L is the Lorentzian width and w_G is the Gaussian width.

Propagation of uncertainty for frequency differences, used to calculate the uncertainty in peak splittings. Here, σ_{ν_1} and σ_{ν_2} are the standard errors from the fit.

$$\sigma_{\Delta\nu} = \sqrt{(\sigma_{\nu_1})^2 + (\sigma_{\nu_2})^2} \tag{9.1}$$

$$\sigma = \sqrt{\frac{1}{N-1} \sum_{i=1}^{N} (x_i - \bar{x})^2} \tag{9.3}$$

Standard deviation for a sample, used to represent spread in repeated measurements.

$$f(x) = A \cdot \exp\left(-\frac{(x-\mu)^2}{2\sigma^2}\right) \tag{9.4}$$

Gaussian function used in peak fitting to model signal response. Parameters include amplitude A, center μ, and width σ.

C Laser Setup

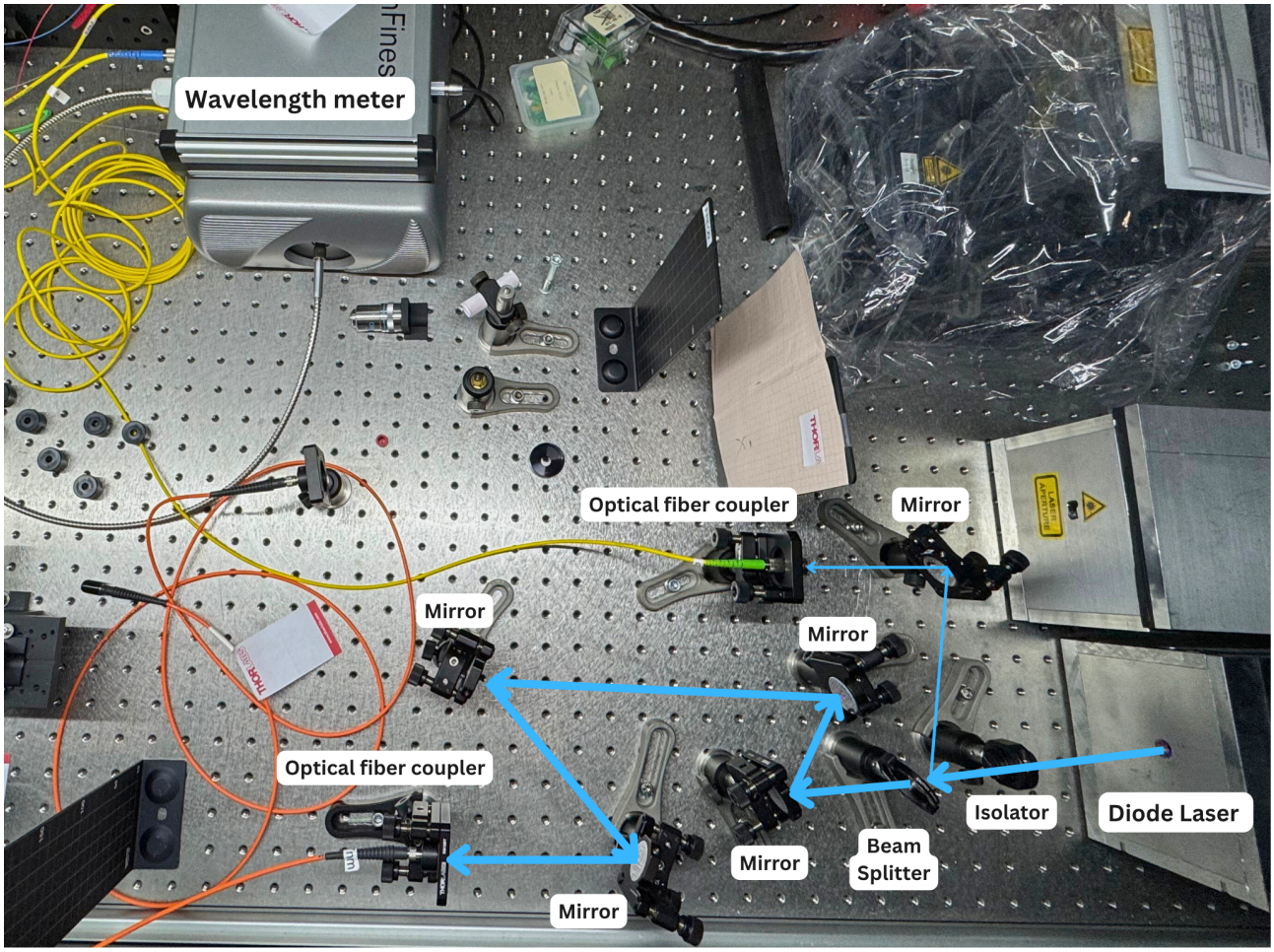

Figure 12: Picture of the Laser Setup analyzed in Figure 5

D Supplementary Spectra for Different Rotational Transitions

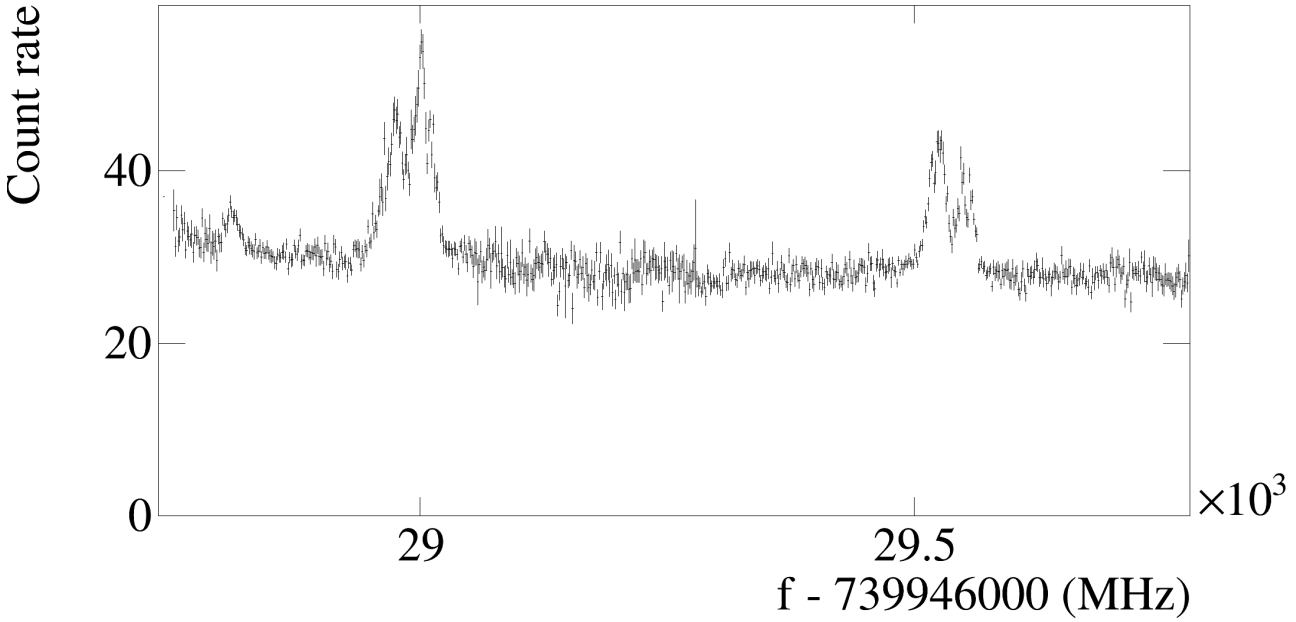

Figure 13: Spectrum of different rotational N levels

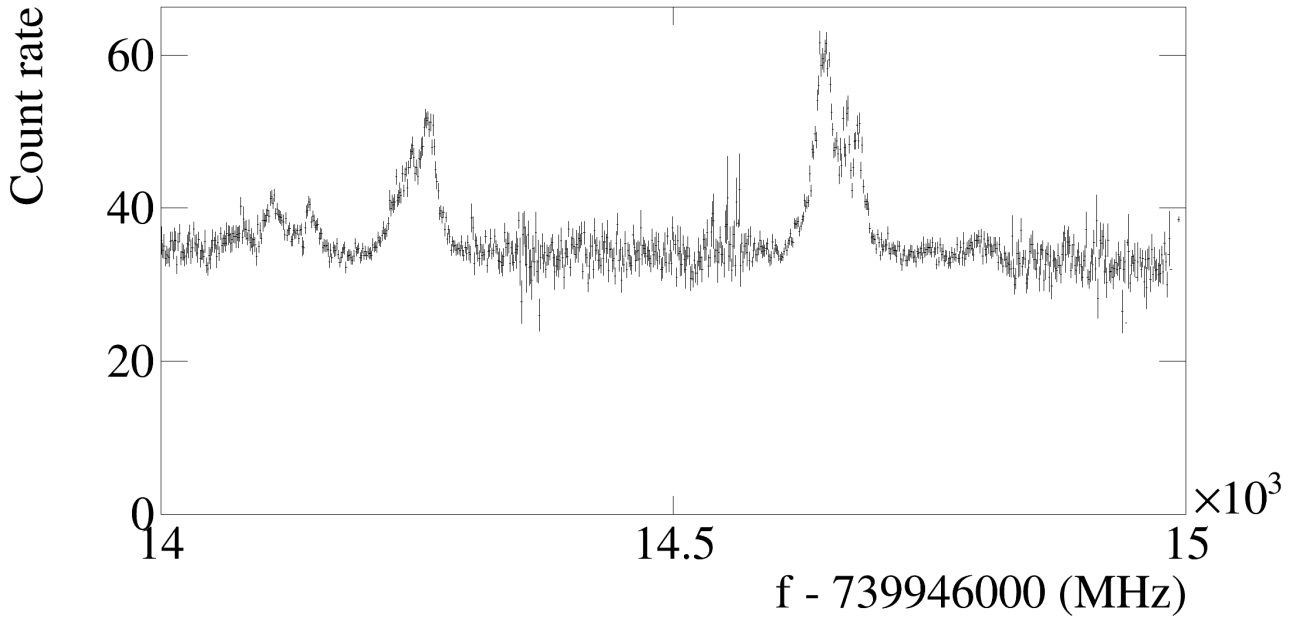

Figure 14: Spectrum of different rotational N levels